Inverse design approach to hole doping in ternary oxides: Enhancing *p*-type conductivity in cobalt oxide spinels

J. D. Perkins,* T. R. Paudel, A. Zakutayev, P. F. Ndione, P. A. Parilla, D. L. Young, S. Lany, D. S. Ginley, and A. Zunger†
National Renewable Energy Lab, Golden, Colorado 80401, USA

N. H. Perry, Y. Tang, M. Grayson, and T. O. Mason
Northwestern University, Evanston, Illinois 60208, USA

J. S. Bettinger, Y. Shi, and M. F. Toney
SLAC National Accelerator Laboratory, Menlo Park, California 94025, USA
(Received 30 September 2011; published 14 November 2011)

Holes can be readily doped into small-gap semiconductors such as Si or GaAs, but corresponding *p*-type doping in wide-gap insulators, while maintaining transparency, has proven difficult. Here, by utilizing design principles distilled from theory with systematic measurements in the prototype A_2BO_4 spinel Co_2ZnO_4, we formulate and test practical design rules for effective hole doping. Using these, we demonstrate a 20-fold increase in the hole density in Co_2ZnO_4 due to extrinsic (Mg) doping and, ultimately, a factor of 10^4 increase for the inverse spinel Co_2NiO_4, the $x = 1$ end point of Ni-doped $Co_2Zn_{1-x}Ni_xO_4$.

DOI: 10.1103/PhysRevB.84.205207 PACS number(s): 71.55.−i, 71.15.−m, 72.80.Ga

I. INTRODUCTION

The ability to significantly shift the Fermi energy by introducing free carriers into insulators underlies a rich diversity of observed physical phenomena. These include insulator-to-metal transitions in doped semiconductors,[1] doping-induced high-temperature superconductivity in $La_{2-x}Ba_xCuO_4$ and related layered copper oxides,[2] electrochromic effects induced by doping in WO_3,[3] electrical transport in the doped semiconductors underlying modern electronics, and the phenomenon of transparent conductors which combine metallicklike conduction with nearly perfect visible-spectrum transparency.[4] Yet, the basic dopability of wide-gap insulators has yet to develop into a systematic, predictive science. Indeed, whereas semiconductors with band gaps of 1–2 eV such as Si or GaAs can be readily doped either *n* or *p* type, wider-gap oxides with gaps exceeding 3 eV such as ZnO or NiO can generally only be doped by one carrier type (e.g., *n* for ZnO and *p* for NiO). And, while most wide-gap materials cannot be doped at all, *n*-type doping of certain wide-gap binary metal oxides such as ZnO or In_2O_3 is possible even at the level of 10^{20} carriers/cm^3.[5,6] Yet, in spite of significant research efforts, comparably doped *p*-type binary oxides have not been found. Towards this end, multication $(A,B,\ldots)$ oxide insulators and semiconductors such as A_2BO_4 spinels,[7,8] ABO_3 perovskites, and ABO_2 delafossites[9] are being widely explored[10] with an emphasis on developing and discovering effective *p*-type oxide materials. Thus far, success has been limited and primarily focused on restricted types of materials (e.g., delafossite $CuAlO_2$) where the initial design focus was improving hole mobility via hybridization of the oxygen orbitals rather than increasing the density of holes in the first place.[9] Accordingly, understanding the key requirements on both the host material, which must tolerate high doping levels, and the dopants necessary to implement broad Fermi energy tuning through doping is central to the discovery and development of new electronic materials.

Here, we apply an iterative theory-guided and experimentally-tested "inverse design" approach to the long-standing problem of *p*-type transparent conductors,[9] in an attempt to develop the scientific basis of this problem. In particular, we will use a three-step approach to inverse design. First, we formulate a number of "design principles," distilled from theoretical calculations, which capture the physical properties necessary to control *n*- and *p*-type dopability. Second, we use high-throughput first-principles defect calculations to examine a class of candidate materials to establish their compliance with the design principles for *p*-type doping. This search across a broad class of materials, metal oxide spinels in this case, is then narrowed down to determine the "best of class" candidate materials. Third, we study specifically the best of class, here $Co_2(Zn,Ni)O_4$, to both verify and optimize the chosen best of class materials through further calculations and corresponding experiments. The value of such a close and iterative coupling of theory with experiment is demonstrated here for the archetype spinel Co_2ZnO_4, where we have increased the conductivity by a factor of 20 via Mg doping and ultimately by a factor of 10^4 for the inverse spinel Co_2NiO_4, the end point of Ni-doped $Co_2Zn_{1-x}Ni_xO_4$. More generally, this coupled approach creates a practical framework for future design principle based search and discovery of effective ternary *p*-type oxides. Indeed, this work is as much about the development of this general and purposeful design principle based approach to materials development as it is about the specific material results found for *p*-type doped cobalt oxide spinels.

II. METHODS

A. Theory methods

Defects enthalpy of formation is calculated by using the density functional supercell approach. Density functional theory (DFT) band structure approach as implemented in VASP code[11] is used with projector augmented wave (PAW) [12] Perdew-Burke-Ernzerhof (PBE) pseudopotential.[13] Exchange and correlation effects beyond generalized gradient

approximation (GGA) are treated in rotationally invariant GGA+U formalism,[13,14] with the onsite Coulomb interaction (U) determined in such a way that it correctly reproduces relative stability of competing binaries.[15] In a supercell approach defect calculation is performed using a 56-atom cubic cell with $2 \times 2 \times 2$ Monkhorst-Pack[16] k points with kinetic energy cutoff of 300 eV and oxygen soft pseudopotentials.

The chemical potential involved is determined using the thermodynamic consideration that a compound exists and all other possible binaries and elemental phases do not exist under a given growth condition. Energy of formations are calculated assuming thermodynamic equilibrium.

The calculated enthalpy of formation includes the corrections[17] due to the image charges, potential alignment, and band filling effects. The dielectric constants necessary in the image charge correction are calculated using the density functional perturbation approach.[18] The number of defects are calculated by minimizing the Gibbs free energy with respect to the number of defects assuming formation enthalpy is independent of the number of defects. The number of defects depends upon the Fermi energy, whereas the Fermi energy itself depends upon the number of carriers, part of which are coming from the ionized defects, so we determine self-consistently the defect density, Fermi energy, and carrier density requiring overall charge neutrality.

B. Experimental methods

Thin-film composition gradient samples ("libraries") of Co-Zn-Ni-O were grown on 2 in. $\times$ 2 in. fused silica glass substrates by rf sputtering from separate targets of CoO, ZnO, and NiO.[19] The sputter sources were inclined at $\sim 30^\circ$ to the substrate normal to achieve a two-dimensional (2D) composition gradient. The chamber base pressure was 10^{-7}–10^{-6} Torr prior to deposition. Films were deposited in a 50/50 O_2/Ar gas mix at a total pressure of 20 mTorr. To cover the full Co_3O_4-Co_2ZnO_4-Co_2NiO_4 ternary composition spread, the relative power on the CoO, ZnO, and NiO sources is varied with a constant total power of 150 W. For each library, the 240-min deposition is preceded by a 30-min burn in. Additional, single-composition Co_2ZnO_4 and Co_2NiO_4 samples were grown by pulsed laser deposition (PLD) on 100-oriented $SrTiO_3$ substrates heated to 350 °C placed 7 cm from the targets in a chamber with 10^{-10} atm base pressure filled with 2.6×10^{-6} atm of oxygen without addition of argon. Co_2ZnO_4 and Co_2NiO_4 targets with Ni/(Ni + Co) = 0.33, 0.38, 0.43 were ablated using a 248-nm excimer laser beam with 2.5 J/cm^2 energy density and 10 Hz repetition rate.

Materials analysis focused on measuring a fixed set of 44 locations on each substrate in a 4 row by 11 column format. The electrical, optical, and structural analysis all focused on the same 44 points on each library, allowing for combinatorial analysis of the results. The rows were located 12.5 mm apart and the columns were 4 mm apart. X-ray fluorescence mapping was utilized to measure the relative Co:Ni:Zn atomic ratio and thickness. Sheet resistance values were characterized with automated four-point probe mapping. Crystallinity and phase composition were measured by x-ray diffraction (XRD) in a mapping fashion using a large Bruker diffractometer equipped with a 2D area detector.[20]

Bulk and powder samples of $Zn_xCo_{3-x}O_4$ and Mg- and Ni-substituted $Zn_xCo_{3-x}O_4$ were fabricated using an aqueous route, in order to mix cations at an atomic level more rapidly than can be achieved by conventional solid state processing at low temperatures. For the $Zn_xCo_{3-x}O_4$ samples, stoichiometric amounts of Co nitrate hexahydrate, 99.999%, and Zn nitrate hexahydrate, 99.998% (both Alfa Aesar, Ward Hill, MA) were dissolved in de-ionized water at room temperature to yield nominal cation ratios, Co/(Zn + Co), ranging from 0.667 to 1. For Mg- and Ni-substituted samples, the same approach was applied with the addition of Mg nitrate hexahydrate, 99.999%, or Ni nitrate hexahydrate, 99.9985% (again Alfa Aesar, Ward Hill, MA).

The mixed nitrate solutions were stirred at 40 °C–50 °C to distribute the cations and evaporate most of the water, taking $\sim$8 h. Then the concentrated solutions were heated at 1 °C–2 °C/min to 390 °C in air in a box furnace in a fume hood to burn out residual water and nitrogen oxides. For low temperature powder samples, the resulting cobalt zinc oxide powders were annealed for 48 h at 390 °C or 500 °C in air and quenched in air. To fabricate higher temperature bulk samples, these powders were ground with an agate mortar and pestle, pressed uniaxially at 125 MPa into pellets, sintered in air for 60 h at 800 °C, and quenched in air. Phase purity was confirmed by x-ray diffraction.

Electrical characterization of the bulk, sintered pellets was performed using room temperature four-point dc conductivity (C4S 4-Point Probe, Cascade Microtech, Inc., Beaverton, OR), ac-impedance spectroscopy (HP 4192A Impedance Analyzer, Agilent Technologies, Santa Clara, CA), and a custom-built Seebeck coefficient analyzer operating at $T_{ave} =$ 40 °C. Room temperature conductivities of powders were determined using the powder-solution-composite technique,[21] where multiple solution-powder composites were fabricated from each powder, measured using impedance spectroscopy, and then analyzed using effective medium theories (Bruggeman Asymmetric and Maxwell-Wagner models[22]).

Anomalous x-ray diffraction (AXRD) measurements to determine the site occupancy were performed at the Stanford Synchrotron Radiation Lightsource (SSRL) beamline 2-1 on both sputtered and PLD-grown Co-Zn-O spinel films as well as bulk powders. Diffraction measurements were performed with x-ray energies varying from 7200 to 8200 eV to probe the Co K edge and from 9160 to 10160 eV to probe the Zn K edge. Slits were used to define the diffracted beam acceptance (1 mm) and a vortex detector was used to collected the diffracted x ray. For the bulk powders, we performed θ–2θ measurements, while for the thin films we fixed θ to be at grazing incidence ($\sim 1^\circ$) while rotating 2θ to a Bragg peak. This maximized the amount of sample that we probed and thus the signal-to-noise ratio. We focused on the 222 and 422 Bragg reflections which are sensitive to only octahedral (O_h) and tetrahedral (T_d) cations in a spinel, respectively.[23]

The AXRD data were quantified using Matlab simulations. For each sample we examined four data sets: Co and Zn K edges for the 222 and 422 Bragg peaks. The data sets were fit simultaneously to determine an inversion parameter (υ) representing the deviation from the predicted normal spinel stoichiometry.

The Seebeck coefficient of PLD-grown Co_2ZnO_4 and Co_2NiO_4 films was measured at room temperature as detailed in Ref. 24. The Hall effect was measured at room temperature using a Van der Pauw method[25] and a variable magnetic field up to 15 T with a 1.7-Hz alternating current source using lock-in techniques, and averaging four up-and-down magnetic field sweeps of both polarities. The data between 0 and 1 T have been removed as they represent purely instrumental noise.

III. DESIGN AND REALIZATION OF *p*-TYPE TRANSPARENT CONDUCTING OXIDE: THE THREE STEPS

We have applied the three-step inverse design approach to the challenging problem of increasing the hole concentration in *p*-type transparent conductors. In particular, first is the formulation and application of general design principles to select a promising class of materials. Second, high-throughput calculations are used to select the best candidate materials. Then third, further calculations and corresponding experiments are used to verify and optimize the chosen best of class materials. Each of these steps is described in more detail below.

A. Step 1: Formulate and apply design principles for *p*-type doping

The following four design principles must be achieved in order to create *p*-type transparent conductors.

(1) *Minimize hole killers*. For oxide base materials this generally requires a low concentration (i.e., high formation energy) of oxygen vacancies which are normally donors (hole killers), as well as a low concentration of antisite defects of the high-valent metal on the low-valent site. If the concentration of potential hole killers is not low, it is then necessary to design such donor transition levels to be resonant inside the valance band, in which case they are electrically inactive and so cause no harm to holes even if they are abundant. This latter special case has been recently termed "doping type II".[26]

(2) *Maximize hole producers*. This can imply maximizing the number (i.e., minimizing the formation energy) of cation vacancies or of intrinsic antisite defects whereby a low-valent metal substitutes a high-valent site or alternatively by extrinsic doping.

(3) *Enhance mobility*. This entails both reducing the hole effective mass and avoiding bound polaron states. The former condition implies that the valence band maximum should be of bonding or antibonding character to increase dispersion (as opposed to being nonbonding). Evaluating the latter condition requires specific calculation.[27]

(4) *Maintain transparency*. Optical gap >3 eV to provide transparency.

These design principles evolved from specific defect calculations. Using first-principles theory to calculate defect formation thermodynamics and defect energy levels in a series of oxides (for details see Sec. II), we establish an initial framework for understanding the problematic introduction and survival of holes in wide-gap oxides. That is, our primary focus here is on design principles 1 and 2 above. For this, the two most important quantities are (i) the enthalpy of formation $\Delta H(\mu,E_F)$ of a defect, which depends both on the relevant chemical potentials μ and the Fermi energy E_F and determines the defect concentration, and (ii) the defect ionization energy $E(Q/Q')$ for ionization from charge state Q to Q', which determines carrier densities. Our three *general findings* are as follows:

First, we searched for oxide groups immune to the formation of intrinsic hole killers (donors) such as oxygen vacancies (V_O). Whereas some antifluorides [e.g., ZrO_2 (Ref. 28)] and some perovskites [e.g., $SrTiO_3$ (Ref. 29)] tend to have a low formation energy for V_O under reducing conditions, we have identified a few standard A_2BO_4 spinels such as Ga_2MgO_4, Al_2MgO_4, and Co_2ZnO_4 that have a large formation enthalpy and/or deep donor levels for oxygen vacancies,[30] leading to a low concentration of hole compensating electrons. Accordingly, we select the broad class of A_2BO_4 spinels as the search space to be considered.

Second, we search for systems likely to accommodate a high concentration of hole producers (acceptors) such as cation vacancies and/or appropriate antisite metal-on-metal substitutions. In *normal* spinel materials $(A^{3+})_2(B^{2+})O_4$, the lower valent B^{2+} cation normally occupies the tetrahedral (T_d) site and the higher valent A^{3+} cation the octahedral (O_h) site. Such ground-state site occupation creates fully occupied bands which render the material insulating. Cation cross-substitution (finite temperature off-stoichiometry) can lead, however, to the formation of free carriers. For example, a lattice defect corresponding to substitution of a high-valent cation onto a normally low-valent lattice site ($A^{3+}_{T_d}$) would create a donor, potentially capable of releasing electrons or killing holes, whereas substitution of a low-valent cation onto a normally high-valent site ($B^{2+}_{O_h}$) would produce an acceptor, potentially capable of releasing holes or killing electrons.

Third, given that two-cation oxides offer the potential for antisite defects with *opposing doping tendencies*, it is necessary to design material systems or synthesis conditions that will be free from such potential intrinsic *compensating* structures. For the case of *p*-type oxides, this means that the formation of $A^{3+}_{T_d}$ defects must be suppressed or otherwise neutralized.

B. Step 2: Search materials class for members satisfying design principles

Taking the A_2BO_4 spinels as the initial materials class, high-throughput first-principles calculations (described in Sec. II) on 43 III-II normal spinels were used to identify the major trends controlling their dopability. The result [see Ref. 26)] is the identification of four major doping types in A_2BO_4 spinels with doping type II, which has an active intrinsic acceptor and essentially no intrinsic donor (hole killer), being of particular interest for *p*-type transparent conductors.[26] In particular, it is found that doping type II spinels have electrically inactive A_{T_d} centers because the corresponding $E(0/+)$ ionization level is located inside the valence band, not the band gap, thus converting the would-be donor $A^{3+}_{T_d}$ into electrically neutral $A^{2+}_{T_d}$. Hence, doping type II spinels tend to be *p* type irrespective of the relative concentration of would-be A_{T_d} donors. The 12 identified doping type II spinels are Ir_2MnO_4, Ir_2FeO_4, Ir_2CoO_4, Ir_2ZnO_4, Ir_2MgO_4, Rh_2MnO_4, Rh_2CoO_4, Rh_2MgO_4, Rh_2ZnO_4, Rh_2CdO_4, Co_2ZnO_4, and Co_2CdO_4.[26] Here, considering the high cost of Ir and Rh

along with the toxicity of Cd, we chose Co_2ZnO_4 as a representative doping type II spinel for further study on the issue of enhancing hole concentration. However, for the octahedrally oxygen-coordinated $Co^{3+}d^6$ ions in Co_2ZnO_4, the valence band is expected to be made of nonbonding t_{2g} orbitals with very little dispersion resulting in heavy hole masses as has been confirmed by recent detailed calculations.[8] Nevertheless, as will be shown, Co_2ZnO_4 is an excellent test material for studying the general factors controlling hole doping in multication oxides.

C. Step 3: Verify and optimize best of class materials

1. Verify Co_2ZnO_4 is doping type II spinel

A naturally low oxygen vacancy concentration was one reason for selecting general A_2BO_4 spinels as our initial materials class. This is confirmed for Co_2ZnO_4 in Fig. 1(a), where V_O is seen to have a formation enthalpy of 2.8 eV in air at 800 °C and a very deep double donor $E(0/{+}{+})$ transition at 1.94 eV below the conduction band minimum, leading to a practically negligible free electron concentration due to such anion vacancies.

Further, for the spinel Co_2ZnO_4, the calculations presented in Fig. 1(a) show that whereas the formation energy for cation vacancies (V_{Co}, V_{Zn}) is high, 2.5–3.5 eV, that for metal-on-metal antisites is much lower, being ~0 eV for Co on Zn (Co_{Zn}) and 1.3 eV for Zn on Co (Zn_{Co}), making such defects the dominant intrinsic defects. This is illustrated in

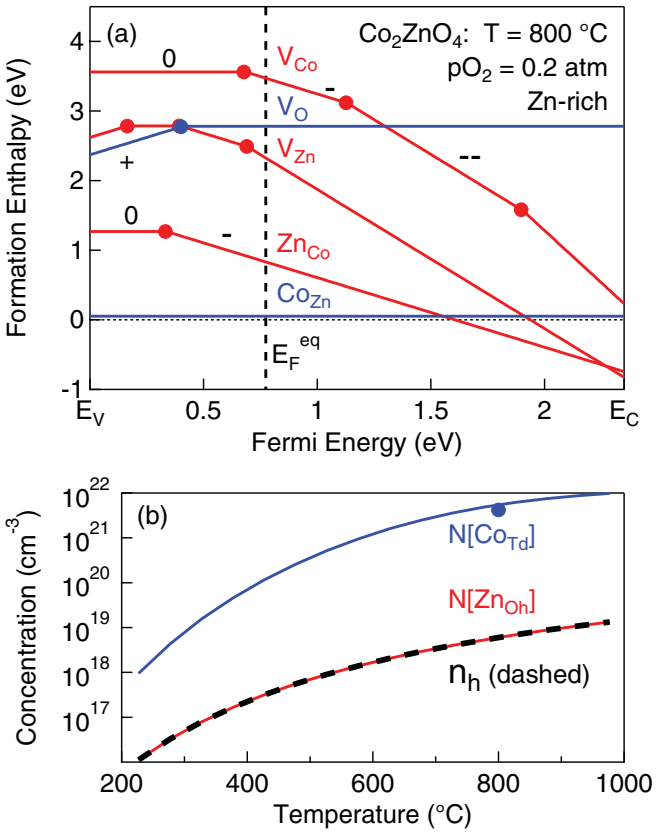

FIG. 1. (Color) Bulk equilibrium Co_2ZnO_4 under Zn-rich conditions at $pO_2 = 0.2$ atm: (a) Calculated formation enthalpy of native defects at $T = 800$ °C. (b) Calculated defect and hole concentrations.

Fig. 1(b), which shows the calculated Co_{Zn} and Zn_{Co} defect concentrations. $N[Co_{T_d}]$ is two to three orders of magnitude higher than $N[Zn_{O_h}]$, making Co_2ZnO_4 inherently Co rich even when synthesized under Zn-rich conditions. These defect concentrations along with their respective specific ionization energy levels, discussed next, determine the material's free-carrier density.

For a doping type II spinel, the potential intrinsic donor (hole killer) A_{T_d} should be electrically inactive and $B^{2+}_{O_h}$ should be an intrinsic acceptor. Figure 1(a) shows that the formation energy of Co_{Zn} (A_{T_d}) does not have a "break" corresponding to a change $E(0/+)$ in defects ionization state within the band gap region. Indeed, for Co_{Zn}, the donor level is *below* the valence band maximum (E_V) at $E_V - 0.22$ eV. Thus, this antisite cannot destroy holes if the Fermi energy is in the band gap. Further, for Co_2ZnO_4, the hole producing $B^{2+}_{O_h}$ (Zn_{O_h}) antisite level is at $E_V + 0.34$ eV making it a reasonably shallow intrinsic $E(0/-)$ acceptor level as evident from the calculated intrinsic hole concentration of $\sim 6\times10^{18}/\text{cm}^3$ at 800 °C [dashed line in Fig. 1(b)]. This confirms that Co_2ZnO_4 is a doping type II spinel. Hence, a key prediction is that given such unopposed hole formation in Co_2ZnO_4 and other similar doping type II spinels, p-type doping is limited only by the ability to find suitably shallow and soluble acceptors, either intrinsic, such as $B^{2+}_{O_h}$, or extrinsic.

We now present experimental results to confirm these calculated results. For the best comparison to these equilibrium calculations, we concentrate initially on *equilibrium conditions*, i.e., the chemical potentials of oxygen, Co, and Zn corresponding to the stable Co_2ZnO_4 phase without precipitates of ZnO or Co_3O_4 secondary phases. Accordingly, we choose *bulk* samples grown in air at temperatures of 390 °C–800 °C by sintering metal oxide mixtures derived from stoichiometric, aqueous metal nitrates.[31] The calculated antisite concentrations [solid lines in Fig. 1(b)] are compared with the experimental $N[Co_{T_d}]$ [blue circle in Fig. 1(b)] as measured by anomalous x-ray diffraction in a sample grown under corresponding Zn-rich conditions and quenched from 800 °C. The experimental value for $N[Zn_{O_h}]$ is below the detection limit of $10^{20}/\text{cm}^3$. There is substantial agreement with the predictions from theory, namely that $N[Co_{T_d}] \gg N[Zn_{O_h}]$. The Seebeck coefficient measured at 40 °C is $+358$ μV/°K showing p-type conductivity. The predicted equilibrium hole concentration for samples grown in air at 800 °C is $n_h = 6\times10^{18}/\text{cm}^3$ [Fig. 1(b)] which agrees with the measured room temperature conductivity $\sigma = 0.007$ S/cm for this $Co_{2.4}Zn_{0.6}O_4$ bulk sample assuming a mobility $\mu = 0.007$ cm^2/V s, which, as we will show later, is reasonable for these materials. We conclude that despite the much larger concentration of the would-be-hole killer A_{T_d} (Co_{T_d}), Co_2ZnO_4 is actually intrinsically p type, due to the small, but crucial, presence of the hole producer $B^{2+}_{O_h}$ (Zn_{O_h}) and the neutralization of the A_{T_d} to $A^{2+}_{T_d}$.

2. Hole effective mass and optical absorption in Co_2ZnO_4

The selected material, Co_2ZnO_4 satisfies design principles 1 and 2 which are the primary targets of this work. To see if it also qualifies as low hole mass material (design principle 3), we first consider its simple molecular orbital levels. Co is

in an octahedral environment. In octahedral symmetry the t_2 orbitals are nonbonding with lobes pointing in between the oxygen ligands, and are thus expected to yield rather narrow sub-bands with heavy mass. In contrast, the e orbitals are bonding and thus expected to lead to broader bands with lighter mass. In Co_2ZnO_4, Co is a Co^{3+} $d6$ ion having fully occupied spin-up as well as spin-down t_2 orbitals. Thus, unfortunately, the highest occupied state is the nonbonding t_2.

These considerations are borne out by calculations of the density of states at the valence band maximum, showing high effective masses (the calculated effective density of states $N_v = 2\times10^{21}/\text{cm}^3$ at 300 K corresponding to a hole effective mass $m^*\approx 18m_e$). Thus, substantiating the expectation from the simple ligand field theory. Hence, we would not expect the holes in Co_2ZnO_4 to have high mobility. In addition, Co_2ZnO_4 with an absorption coefficient of order 10^4/cm at 1.8 eV (690 nm) is more absorbing than desired for a transparent conductor.[19] Nevertheless, we proceeded with Co_2ZnO_4, as our focus in this work is on enhancing the carrier concentration so as to test our understanding and control of the newly developed design principles.

IV. THREE STRATEGIES TO ENHANCE DOPING IN Co_2ZnO_4

Having formulated design principles, applied them to search a group of candidate materials, and then narrowed down to one material of interest, we next explore how these design principles can help enhance the carrier density. Specifically, we consider, both theoretically and experimentally, three strategies to increase the intrinsic hole concentration in p-type Co_2ZnO_4. They are (i) enhance the intrinsic acceptor concentration via nonequilibrium growth, (ii) extrinsic metal doping on the cation site, and (iii) induce the inverse spinel structure.

A. Strategy 1: Enhance $B^{2+}_{O_h}$ concentration via nonequilibrium growth

To evaluate the hole producing potential of excess, above-equilibrium Zn incorporation, the site occupancies were calculated in the same way as for the equilibrium results of Fig. 1. However, the Zn chemical potential is now allowed to be higher than would yield ZnO phase separation under equilibrium conditions. The solid lines in Fig. 2(a) show the calculated site occupancies vs the relative Zn content $\lambda = \text{Zn}/(\text{Zn} + \text{Co})$ ranging from Zn poor ($\lambda < 0.33$) through stoichiometric ($\lambda = 0.33$) and Zn rich ($\lambda > 0.33$). When excess Zn is incorporated ($\lambda > 0.33$), it must go to the O_h site and hence the Zn_{O_h} site occupancy would increase linearly with excess Zn content. Hence, if excess Zn can be incorporated, then a substantial increase in the hole producing Zn_{O_h} defect is expected.

The samples to test this prediction are thin-film composition gradient combinatorial libraries which were, in this case, grown on glass substrates at $T = 340$ °C and $pO_2 \approx 10^{-5}$ atm by cosputtering from separate ZnO and CoO targets to create samples with intentional Co:Zn composition gradients.[20] The corresponding measured site occupancies [open symbols in Fig. 2(a)] agree very well with predictions. Hence, as surmised

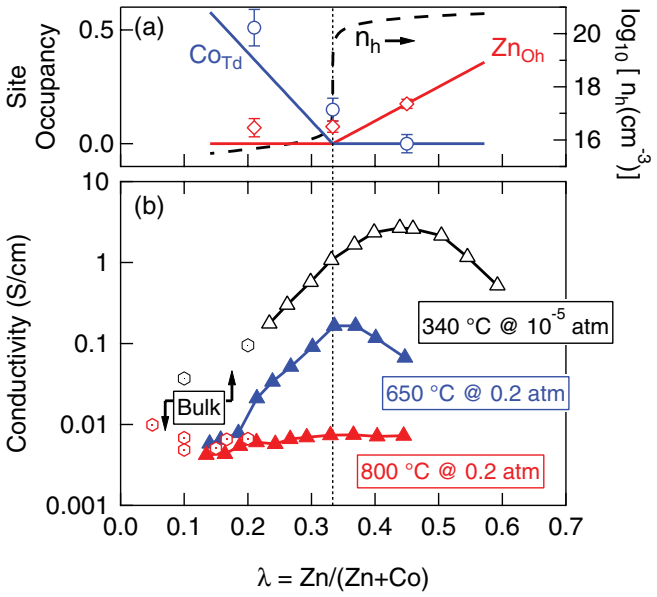

FIG. 2. (Color) Nonequilibrium Co_2ZnO_4 at $T = 340$ °C and $pO_2 = 10^{-5}$ atm: (a) Site occupancy and hole concentration (lines for theory and symbols for experiment). (b) Conductivity vs relative zinc composition for as-deposited (open triangles) and annealed (solid triangles) thin films as well as bulk ceramic samples (open hexagons).

above, it is possible to enhance the concentration of Zn_{O_h} by using nonequilibrium materials growth. The calculated hole concentration n_h [dashed line in Fig. 2(a)] shows a rapid three orders of magnitude rise when excess Zn is incorporated from $n_h = 2.3\times10^{16}/\text{cm}^3$ at $\lambda = 0.325$ (Zn poor) to $n_h = 3.6\times10^{19}/\text{cm}^3$ at $\lambda = 0.335$ (Zn rich). Hence, even a very small increase in the Zn content above the equilibrium limit is seen to be very beneficial for creating holes.

Figure 2(b) shows the measured electrical conductivity as a function of relative Zn composition for both as-deposited (black line, open triangles) and air-annealed (colored line, solid triangles) thin films as well as bulk ceramic samples (symbols only), demonstrating a significant conductivity increase in the thin films with $\sigma_{\text{Max}} \sim 5$ S/cm at $\lambda \approx 0.44$ compared to the bulk ceramic samples with $\sigma_{\text{Max}} \sim 0.1$ S/cm at $\lambda \approx 0.2$. However, the electrical conductivity of the bulk samples agrees with that of the thin-film samples in the composition region of overlap near $\lambda \approx 0.2$. This shows that Zn-rich samples can be grown using nonequilibrium thin-film growth methods and suggests that the excess Zn incorporation significantly increases the conductivity in agreement with the above prediction. Recall that Zn-rich compositions are not possible for the essentially equilibrium bulk samples grown at 800 °C ($\text{N}[\text{Co}_{T_d}] \gg \text{N}[\text{Zn}_{O_h}]$ in Fig. 1(b).

A direct Hall effect measurement of the carrier concentration and type is desirable, but difficult for these low mobility materials, especially in polycrystalline bulk or randomly oriented polycrystalline thin-film form. Accordingly, slightly Zn-rich $Co_{1.98}Zn_{1.02}O_4$ ($\lambda \approx 0.34$) films were grown by PLD in 2 mTorr O_2 at $T_S = 350$ °C on 100-oriented $SrTiO_3$ from a $Co_{1.92}Zn_{1.08}O_4$ target. X-ray diffraction measurements show the films to be 100 oriented. Figure 3 shows the Hall resistivity as a function of the magnetic field with the maximum

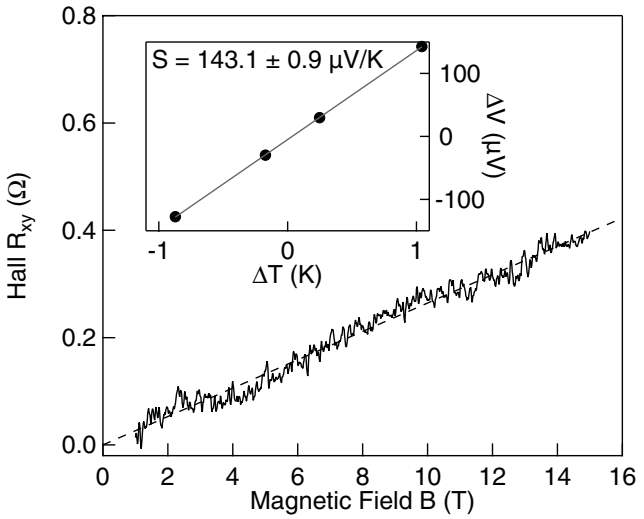

FIG. 3. Hall effect measurement of biaxially textured Co_2ZnO_4 thin film grown on $SrTiO_3$ substrate. Inset: Seebeck effect measurement of same film.

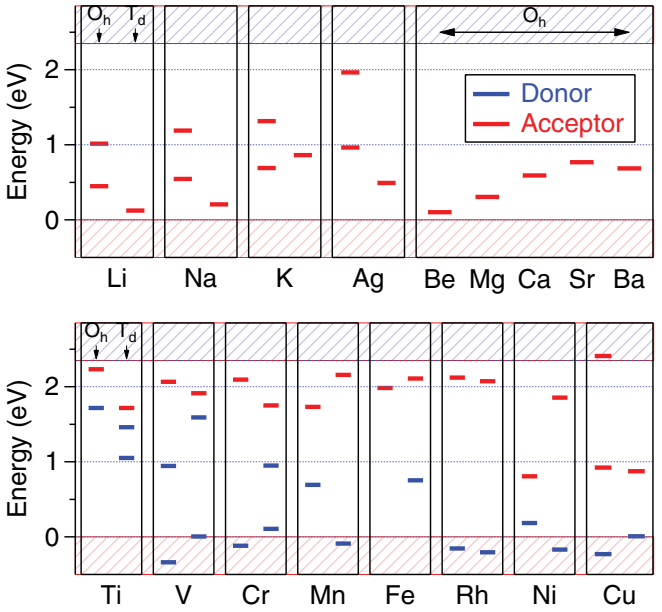

FIG. 4. (Color) Calculated acceptor and donor energy levels for potential extrinsic dopants in Co_2ZnO_4.

applied field of 15 T. The conductivity of this sample is 8.1 S/cm and the positive slope indicates p-type conduction with a hole concentration $p = 1.8\times10^{21}/\text{cm}^3$ and a mobility $\mu = 0.028$ cm^2/V s. The inset shows the measured Seebeck effect for this sample with a positive Seebeck coefficient $S = +143$ μV/K confirming the p-type conduction. These results show that excess Zn incorporation will yield a high carrier concentration consistent with the calculated prediction of Fig. 2(a) which shows $p > 10^{20}/\text{cm}^3$ for Zn-rich samples. However, the mobility is very low, even in oriented thin-film samples grown on single crystal substrate. For comparison, the mobility of conventional n-type transparent conductors is typically 10–50 cm^2/V s, roughly three orders of magnitude higher. Nevertheless, in spite of the low resultant mobility, we find that Strategy 1 of using nonequilibrium growth to enhance the concentration of the native acceptor defect works.

B. Strategy 2: Extrinsic metal dopants to create acceptors

Since Co_2ZnO_4 has no intrinsic hole killers, suitable extrinsic M^{2+} dopants on the O_h (Co) site or M^{1+} dopants on the T_d (Zn) site could be very effective at increasing the hole concentration. Accordingly, we have calculated donor (Fig. 4, blue) and acceptor (red) energy levels on both the O_h and T_d sites for candidate alkali, alkaline earth, and transition metal dopants. Of the 17 considered, Li_{T_d} with acceptor $E(0/-) = E_V + 0.12$ eV and Be_{O_h} with $E(0/-) = E_V + 0.10$ eV have especially low ionization energy levels. However, the toxicity of Be eliminated it from further consideration. For Li doping, Fig. 5 (inset) shows the calculated hole concentration as a function of dopant concentration (η). Li is found to be essentially a perfect dopant with nearly unity activation up to the calculated solubility limit of $\eta_{\text{Li}}^{\text{max}} \approx 0.002$. However, due to the reactivity of Li and difficulty in depositing Li materials by physical vapor deposition (PVD) approaches, it was excluded from further experimental study here. Accordingly, Na_{T_d} and Ag_{T_d} were considered, but their equilibrium solubility was found to be lower than the intrinsic Zn_{O_h} concentration and hence they are not effective dopants. From the remaining choices, the calculated equilibrium hole concentrations [Fig. 5 (inset)] show Mg and Ni to be viable practical dopants. Assuming equal solubility, the calculations show that Ni is about twice as effective a dopant as Mg. This is at first surprising because the acceptor energy level for Mg_{O_h} is $E_V + 0.3$ eV whereas that for Ni_{O_h} is substantially higher at $E_V + 0.8$ eV. However, only ~2%–10% of the Mg goes to the O_h site at low doping levels ($\eta < 0.06$). In contrast, all the Ni goes to the O_h site but with only ~30% activation and the maximum equilibrium solubility is low, $\eta_{\text{Ni}}^{\text{max}}$=0.003.

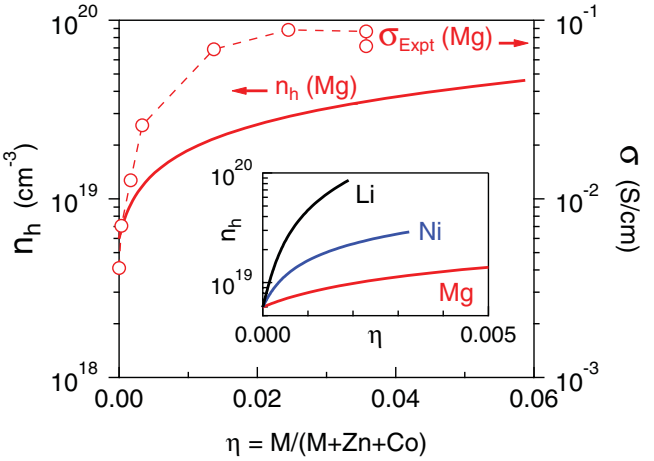

FIG. 5. (Color) Metal doped Co_2ZnO_4 at $T = 800$ °C and $pO_2 = 0.2$ atm. Calculated hole concentration (solid line) and conductivity measured at room temperature (dashed line, open symbols) for Mg-doped Co_2ZnO_4. (Inset) Calculated hole concentration n_h for extrinsic doping of Co_2ZnO_4 with Li, Ni, and Mg.

Figure 5 shows the predicted hole concentration n_h (solid line) as a function of Mg content at $T = 800$ °C and $pO_2 = 0.2$ atm, the growth conditions of the bulk samples, as well as the measured room temperature conductivity of bulk samples (dashed line with symbols). The qualitative agreement is good regarding the overall increase in conductivity with increasing Mg content. Experimentally, a factor of 20 increase in the conductivity from $\sigma \approx 0.04$ S/cm to $\sigma \approx 0.9$ S/cm is observed for these Co-rich ($Co_{2.7}Zn_{0.3}O_4$ for Mg-free sample) bulk ceramic samples. Quantitatively, the hole concentration and conductivity axis in Fig. 5 are equivalent as plotted for a mobility $\mu = 0.006$ cm^2/V s, essentially identical to the $\mu = 0.007$ cm^2/V s found for bulk intrinsic Co_2ZnO_4 (Fig. 1). Hence, we find that Strategy 2 of seeking appropriate extrinsic dopants with higher equilibrium solubility than the intrinsic antisite Zn_{O_h} defect works.

C. Strategy 3: Induce the "inverse spinel" phase to maximize divalent cations on octahedral site

For a *normal* spinel crystal structure, all the divalent B^{2+} cations occupy the T_d site at $T = 0$. The ultimate limit of maximal $B^{2+}_{O_h}$ site defects can be achieved if the *normal* spinel can be transformed into an *inverse* spinel structure, where the divalent cation resides exclusively on the O_h site, becoming the ultimate $B^{2+}_{O_h}$ acceptor. Co_2NiO_4 is a known inverse spinel[32] and can be considered the end point of Ni on O_h site doped Co_2ZnO_4, albeit one where octahedral Ni displaces the tetrahedral Zn indirectly by way of Co moving from the O_h to the T_d site. To this end, thin-film Ni-Co-Zn-O composition-gradient samples spanning the entire pseudoternary composition region from Co_3O_4 to Co_2ZnO_4 to Co_2NiO_4 were grown by ternary cosputtering. Figure 6 shows the conductivity of these ternary samples and

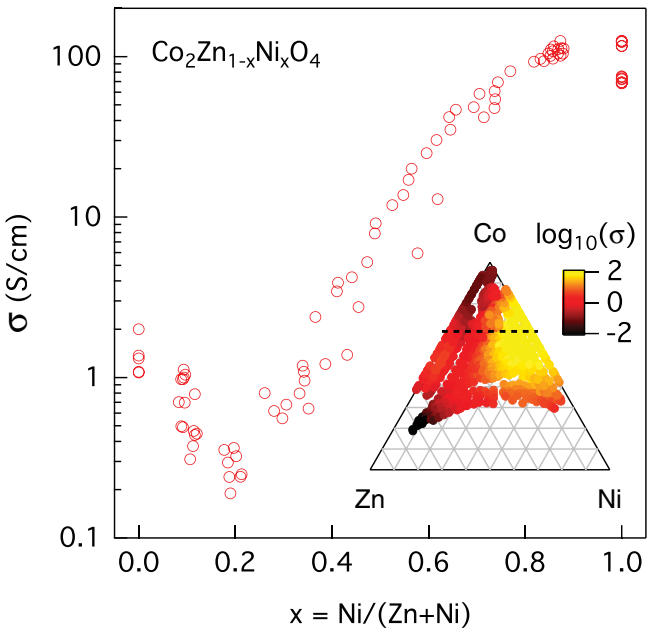

FIG. 6. (Color) Room temperature conductivity of Co-Zn-Ni-O thin films. Inset shows ternary graph with logarithmic color scale. Main panel shows conductivity on line from Co_2ZnO_4 to Co_2NiO_4. Films grown at $T = 340$ °C and $pO_2 = 10^{-5}$ atm.

the dominant result is a factor of 100 increase in the electrical conductivity with increasing Ni content from Co_2ZnO_4 to Co_2NiO_4 with $\sigma \approx 100$ S/cm. This qualitatively agrees with our above discussion of the inverse spinel Co_2NiO_4 being the end point of Ni-on-O_h site doped Co_2ZnO_4. However, it appears to contradict the calculated equilibrium Ni solubility limit of $\eta^{max}_{Ni} = 0.003$ [Fig. 5 (inset)], but as discussed above, the thermodynamically expected secondary phase formation can be suppressed in nonequilibrium growth methods such as sputtering. To confirm the carrier type, oriented Co_2NiO_4 thin films were grown on single crystal $SrTiO_3$ substrates for Seebeck measurements. The positive Seebeck coefficient $S = +13$ μV/K confirms the expected p-type conduction in Co_2NiO_4. Hence, we find that Strategy 3 of inducing the inverse spinel phase works.

V. DISCUSSION AND CONCLUSIONS

We conclude by summarizing the pertinent design principles and the resultant design rules (DRs) formulated and tested here for p doping of oxides.

(i) *Avoid intrinsic hole-killers* resulting in two specific design rules: DR1: Select materials where V_O is difficult to form; and DR2: Select multication materials where the hole-killer high-valent (HV) on low-valent (LV) substitution is electrically inactive even if it is abundant.

(ii) *Increase concentration of hole producers (acceptors).* This can be accomplished by DR3: Increase metal site disorder at fixed A:B cation composition so as to enhance *intrinsic* LV-on-HV by using nonequilibrium growth or materials with a natural tendency to form the inverse spinel structure; DR4: Utilize nonequilibrium growth targeted specifically to incorporate excess (beyond equilibrium) LV cations and hence increase concentration of LV-on-HV acceptors; and DR5: Find suitable *extrinsic* LV-on-HV impurities to act as unopposed hole creators. These design principles provide a specific understanding of the factor of 10^4 difference in conductivity between intrinsic equilibrium (bulk) Co_2ZnO_4 ($\sigma \approx 0.01$ S/cm)[33] and thin-film Co_2NiO_4 ($\sigma \approx 100$ S/cm).[34] More importantly, they provide a general strategy and framework for both understanding known and developing new multication oxide p-type electronic materials. Further, the iterative inverse design approach demonstrated here can be applied in general to new materials discovery and development.

ACKNOWLEDGMENTS

This work is supported by the U.S. Department of Energy, Office of Science, Office of Basic Energy Sciences under Contract No. DE-AC36-08GO28308 to NREL. The "Center for Inverse Design" is a DOE Energy Frontier Research Center. Portions of this research were carried out at the Stanford Synchrotron Radiation Lightsource user facility, operated by Stanford University on behalf of the U.S. Department of Energy, Office of Basic Energy Sciences.

*john.perkins@nrel.gov
†Present address: University of Colorado, Boulder, Colorado 80309, USA.

[1] N. F. Mott, *Metal-Insulator Transitions* (Taylor and Francis, London, 1990).
[2] J. G. Bednorz and K. A. Muller, Z. Phys. B: Condens. Matter **64**, 189 (1986).
[3] S. K. Deb, Philos. Mag. **27**, 801 (1973).
[4] D. S. Ginley and C. Bright, MRS Bull. **25**, 15 (2000).
[5] S. Lany and A. Zunger, Phys. Rev. Lett. **98**, 045501 (2007).
[6] S. B. Zhang, S. H. Wei, and A. Zunger, Phys. Rev. B **63**, 075205 (2001).
[7] Another widely used way of writing the spinel chemical formula is AB_2O_4. We write however, A_2BO_4 which is common for spinels with formal cation valencies $Z_A = 2$ and $Z_B = 4$ such as Mg_2TiO_4. The main reason for our choice is because the work presented here is part of a larger project that treats all A_2BX_4 compounds (not only spinels) in different structure types including olivine Fe_2SiO_4, β-K_2SO_4, or La_2CuO_4 for which A_2BX_4 is the generally used notation.
[8] D. O. Scanlon and G. W. Watson, Phys. Chem. Chem. Phys. **13**, 9667 (2011).
[9] H. Kawazoe, M. Yasukawa, H. Hyodo, M. Kurita, H. Yanagi, and H. Hosono, Nature **389**, 939 (1997).
[10] G. J. Exarhos and X. D. Zhou, Thin Solid Films **515**, 7025 (2007).
[11] G. Kresse and D. Joubert, Phys. Rev. B **59**, 1758 (1999).
[12] P. E. Blochl, Phys. Rev. B **50**, 17953 (1994).
[13] J. P. Perdew, K. Burke, and M. Ernzerhof, Phys. Rev. Lett. **77**, 3865 (1996).
[14] S. L. Dudarev, G. A. Botton, S. Y. Savrasov, C. J. Humphreys, and A. P. Sutton, Phys. Rev. B **57**, 1505 (1998).
[15] S. Lany, Phys. Rev. B **78**, 245207 (2008).
[16] H. J. Monkhorst and J. D. Pack, Phys. Rev. B **13**, 5188 (1976).
[17] S. Lany and A. Zunger, Phys. Rev. B **78**, 235104 (2008).
[18] S. Baroni and R. Resta, Phys. Rev. B **33**, 7017 (1986).
[19] A. Zakutayev, J. D. Perkins, P. A. Parilla, N. E. Widjonarko, A. K. Sigdel, J. J. Berry, and D. S. Ginley, MRS Communications (2011), doi: 10.1557/mrc.2011.9.
[20] M. P. Taylor, D. W. Readey, C. W. Teplin, M. F. A. M. van Hest, J. L. Alleman, M. S. Dabney, L. M. Gedvilas, B. M. Keyes, B. To, P. A. Parilla, J. D. Perkins, and D. S. Ginley, Macromol. Rapid Commun. **25**, 344 (2004).
[21] M. D. Irwin, B. Buchholz, A. W. Hains, R. P. H. Chang, and T. J. Marks, Proc. Natl. Acad. Sci. USA **105**, 2783 (2008).
[22] D. S. McLachlan, M. Blaszkiewicz, and R. E. Newnham, J. Am. Ceram. Soc. **73**, 2187 (1990).
[23] E. Kravtsov, D. Haskel, A. Cady, A. Yang, C. Vittoria, X. Zuo, and V. G. Harris, Phys. Rev. B **74**, 104114 (2006).
[24] D. L. Young, T. J. Coutts, and V. I. Kaydanov, Rev. Sci. Instrum. **71**, 462 (2000).
[25] L. J. Van Der Pauw, Philips Res. Rep. **13**, 1 (1958).
[26] T. R. Paudel, A. Zakutayev, S. Lany, M. d'Avezac, and A. Zunger, Adv. Funct. Mater. (2011), doi: 10.1002/adfm.201101469.
[27] A. R. Nagaraja, N. H. Perry, T. O. Mason, Y. Tang, M. Grayson, T. R. Paudel, S. Lany, and A. Zunger, J. Am. Ceram. Soc. (2011), doi: 10.1111/j.1551-2916.2011.04771.x.
[28] J. X. Zheng, G. Ceder, T. Maxisch, W. K. Chim, and W. K. Choi, Phys. Rev. B **75**, 104112 (2007).
[29] M. Choi, F. Oba, and I. Tanaka, Phys. Rev. Lett. **103**, 185502 (2009).
[30] A. Zunger, Appl. Phys. Lett. **83**, 57 (2003).
[31] T. O. Mason, G. B. Gonzalez, D. R. Kammler, N. Mansourian-Hadavi, and B. J. Ingram, Thin Solid Films **411**, 106 (2002).
[32] P. D. Battle, A. K. Cheetham, and J. B. Goodenough, Mater. Res. Bull. **14**, 1013 (1979).
[33] M. Dekkers, G. Rijnders, and D. H. A. Blank, Appl. Phys. Lett. **90**, 021903 (2007).
[34] C. F. Windisch, G. J. Exarhos, K. F. Ferris, M. H. Engelhard, and D. C. Stewart, Thin Solid Films **398**, 45 (2001).